Article

In situ study of graphene oxide quantum dot-MoS$_x$ nanohybrids as hydrogen evolution catalysts

Marco Favaro [1,†], **Mattia Cattelan** [1,‡], **Stephen W. T. Price** [2], **Andrea E. Russell** [3], **Laura Calvillo** [1,*], **Stefano Agnoli** [1] **and Gaetano Granozzi** [1]

[1] Dipartimento di Scienze Chimiche, Università di Padova, Via Marzolo 1, 35131 Padova, Italia

[2] Finden Ltd, 1.12 Building R71, Harwell Campus, Oxfordshire, OX11 0QZ, UK

[3] School of Chemistry, University of Southampton, Highfield, Southampton SO17 1BJ, UK

[†] Present address: Helmholtz-Zentrum Berlin für Materialien und Energie GmbH, Institute for Solar Fuels, Hahn-Meitner-Platz 1, D-14109 Berlin, Germany

[‡] Present address: School of Chemistry, University of Bristol, Cantocks Close, Bristol BS8 1TS, UK

[*] Correspondence: laura.calvillolamana@unipd.it

Abstract: Graphene quantum dots (GOQDs)-MoS$_x$ nanohybrids with different MoS$_x$ stoichiometries (x = 2 and 3) were prepared in order to investigate their chemical stability under hydrogen evolution reaction (HER) conditions. Combined photoemission/electrochemical (XPS/EC) measurements and *operando* X-ray absorption spectroscopy (XAS) were employed to determine the chemical changes induced on the MoS$_x$-based materials as a function of the applied potential. This *in situ* characterization indicates that both MoS$_2$ and MoS$_3$ materials are stable under operating conditions, although sulphur terminal sites in the MoS$_3$ nanoparticles are converted from S-dimer (S_2^{2-}) to S-monomer (S^{2-}), which constitute the first sites where the hydrogen atoms are adsorbed for their subsequent evolution. In order to complete the characterization of the GOQDs-MoS$_x$ nanohybrids, the composition and particle size were determined by X-ray photoemission spectroscopy (XPS), X-ray diffraction (XRD) and Raman spectroscopy; whereas the HER activity was studied by conventional electrochemical techniques.

1. Introduction

The use of hydrogen as an energy carrier in fuel cells (FCs) is one of the most promising energy policies for a rapid transition from fossil fuels to more sustainable energy sources. In this context, it is mandatory to find clean and easy methods for hydrogen production. Most of the hydrogen used today is obtained by steam reforming of methane; however, the H$_2$ produced through this route contains a small amount of carbon monoxide, a poison for Pt-based electrocatalysts, that makes it unsuitable for its direct use in FCs. The production of hydrogen by electrochemical water splitting, exploiting the hydrogen evolution reaction (HER), is therefore gaining importance, also because this alternative production method allows the storage of the electricity intermittently generated by renewable sources and further reduces the dependency on hydrocarbon fuels. Since this reaction is catalytically activated, there is now renewed interest in the development of efficient HER electrocatalysts. Platinum-group-metals (PGMs) are the best candidates as HER electrocatalysts, but they are unsuitable to empower such technology on a large scale, because they are considered critical raw materials.[1,2] Thence nowadays, an intense research activity is underway to test earth abundant elements as HER catalysts, alternative to PGMs based ones, which are capable of operating

43 in water, providing both high current density at a low overpotential, and a sufficient current
44 durability [3,4]. In this context, transition metal chalcogenides (TMCs) (e.g. MoS_2 and other sulfides
45 and selenides) derived nanomaterials represent promising HER catalysts [3,5]. Nevertheless, the
46 mechanism HER activity for MoS_x-based catalysts is still disputed [6]. Most works agree on the key
47 role played by sulfur species in the HER, however, the large variety of different structural building
48 blocks, which are the basis of the many possible crystalline, amorphous or polymeric molybdenum
49 sulfide phases, comprising μ-S^{2-}/μ-S_2^{2-}, terminal η^2-S_2^{2-}, apical S^{2-}, and unsaturated S^{2-}, makes the
50 establishment of direct structure-activity relationships very difficult. Moreover, complex
51 physicochemical changes can be triggered by the reducing electrochemical potential, making the
52 interpretation of the experimental data even more complex. For example, some authors suggested
53 that S^{2-} monomer, typical of the Mo edge in MoS_2, form the most active sites [7]; on the other hand,
54 other works outline the key role of η^2-S_2^{2-} species [8]. It has been also suggested that the removal of
55 sulfur species driven by the reducing potential can produce unsaturated Mo(IV)/Mo(V) species that,
56 via the formation of transient metal hydrides, are the active sites in the evolution of hydrogen [9,10].
57 Very recently, combined experimental and theoretical data suggested that bridging μ-S^{2-} units
58 connecting Mo(V) and Mo(IV) cations exhibit extremely high activity, and that the presence of
59 oxygen in the anion lattice consequent to the etching of sulfur species at reducing potential, is also
60 very beneficial for electroactivity [11,12,13].

61   Given the complexity outlined above, experiments that allow the investigation of materials
62 using *operando* conditions are essential to study the cathodic-triggered formation of MoS_x species. In
63 addition, these measurements should provide a good representation of the ultimate stability of the
64 electrocatalysts under operating conditions. For example, several groups have reported that
65 amorphous MoS_3 is not stable under the operating cathodic conditions [7,8,9], and it is gradually
66 reduced to a sulfur deficient structure very similar to MoS_2. In contrast, other authors have
67 suggested the presence of Mo(V) [9] or alternatively Mo(III) [8], however the presence of
68 unsaturated cation species seems to be a common feature .

69   In the present work, we describe a new synthesis method to prepare graphene quantum dot
70 (nanometric graphene sheets, GOQD)-MoS_x nanohybrids with different MoS_x stoichiometries (x = 2
71 and 3). Graphene based materials have emerged as promising platforms for growing MoS_2 due to
72 their high surface area and good stability [12-14]. We have extended this approach to GOQD since
73 the use of very small graphene sheets (< 5 nm) is optimal for the development of bottom up synthesis
74 protocols, resulting in an intimate interaction between the two phases. The result is an advanced
75 nanocomposite made up by small MoS_x nanoparticles (NPs) with abundant exposed edge sites,
76 highly dispersed and stabilized by a graphene matrix. We have used combined
77 electrochemical/photoemission measurements, as well as *operando* X-ray absorption spectroscopy
78 (XAS), to track the changes experienced by the material under operating conditions. This complete
79 methodological approach allowed us to determine the actual MoS_x species involved in the HER.
80

81 **2. Materials and Methods**

82 *2.1. Synthesis and physicochemical characterization of GOQD-MoS_x nanohybrids*

83   4.3 mg of $(NH_4)_2MoS_4$ were dissolved in 1.6 mL of GOQDs solution (1 mg mL^{-1}) and sonicated
84 for 20 min. Subsequently, 10 μL of Nafion solution (5 wt.% solids in alcohol and water,
85 Sigma-Aldrich) were added to the suspension and sonicated for another 10 min. The synthesis of the
86 GOQDs is detailed in the Supplementary Materials (SM).
87   For the XAS measurements, the electrodes were manufactured by painting the
88 GOQD-$(NH_4)_2MoS_4$ suspension on to carbon paper (TGP-H-60) to obtain a final Mo loading of 1.25
89 mg cm^{-2}. Circular button electrodes of 1.25 cm^2 area were cut and annealed at 250 °C and 700 °C in
90 UHV to obtain the final GOQD-MoS_3 and GOQD-MoS_2 electrodes, respectively.
91   For the XPS/EC measurements, 80 μL aliquots of GOQD-$(NH_4)_2MoS_4$ suspension were drop
92 casted on to a glassy carbon electrode and dried in N_2 atmosphere. The electrodes were introduced

93 into the UHV system and annealed at 250 °C and 700 °C to obtain the final GOQD-MoS$_3$ and
94 GOQD-MoS$_2$ electrodes, respectively.

95 Raman spectra were acquired using a ThermoFisher DXR Raman microscope. The spectra were
96 recorded using a laser with an excitation wavelength of 532 nm (1 mW), focused on the sample with
97 a 50× objective (Olympus).

98 The X-ray diffraction (XRD) characterization was performed with a Philips PW 1729,
99 configured with a glancing angle geometry, operating with Cu Kα radiation (λ = 0.15406 nm)
100 generated at 30 kV and 40 mA. The mean crystallite size was calculated from the MoS$_2$(002) peak
101 using the Scherrer equation: Lc = k·λ/ß·cosθ, where k is the shape factor (k = 0.9), λ is the X-ray
102 wavelength, ß is the line broadening at half the maximum intensity of the peak, and θ is the Bragg
103 angle.

2.2. Electrochemical measurements

105 The electrochemical measurements were conducted in a standard three-electrode
106 electrochemical cell. A glassy carbon rod was used as counter electrode and a saturated calomel
107 electrode (SCE) placed inside a Luggin capillary was used as reference electrode. A 0.5 M H$_2$SO$_4$
108 solution, prepared from high purity reagents (Sigma-Aldrich) and purged with argon gas, was used
109 as supporting electrolyte. All the electrochemical experiments were carried out at room temperature.
110 Ten cyclic voltammograms between +0.3 V and -0.1 V vs RHE at 0.1 V s^{-1} were performed to get a
111 good contact between the electrode and electrolyte and, subsequently, three more scans were
112 measured at 0.020 V s^{-1}. Polarization curves were recorded between +0.2 and -0.3 V vs RHE using a
113 scan rate of 0.005 Vs^{-1}. The third linear sweep voltammetry (LSV) was used to compare the
114 performance of the different catalysts toward the HER.

2.3. Operando X-ray absorption spectroscopy (XAS) measurements

116 An *in situ* electrochemical cell was used to collect XAS data of the MoS$_x$-based catalysts as a
117 function of the applied potential [15] (Figure S1a). The working electrode was held in place by an Au
118 wire contact, a Pt wire served as the counter electrode, and the reference electrode was a mercury
119 mercurous sulfate (Hg/Hg$_2$SO$_4$) electrode (calibrated as +0.697 V vs RHE) that was connected to the
120 cell via a short length of tubing containing the electrolyte. The cell was controlled by an Autolab
121 potentiostat running with NOVA 1.8 Software. The electrolyte was purged with N$_2$ and then
122 pumped through the cell using a peristaltic pump. The samples were prepared as button electrodes
123 (fresh electrodes) and the measurements were carried out at four different fixed potentials.
124 Subsequently, the electrodes were subjected to an accelerated ageing treatment (AAT) (aged
125 electrodes), which consisted of 500 cycles between +0.2 V and -0.25 V vs RHE at 0.050 Vs^{-1}, in order to
126 study the stability of the samples and, then, XAS measurements were performed at the same fixed
127 potentials. The measurements were run in 0.5 M H$_2$SO$_4$ purged with N$_2$. Prior to the XAS
128 measurements, three cyclic voltammograms were collected between 0.3 and -0.1 V vs RHE at 50 mV
129 s^{-1} to clean the surface and ensure fully contact between the electrode and electrolyte. Three further
130 cycles were recorded at 10 mV s^{-1} to ensure that the electrode was stable. A linear scan voltammetry
131 was run to reach the desired potential for the XAS measurements. X-ray adsorption measurements
132 were recorded on beamline B18 at Diamond Light Source (UK) with ring energy of 3 GeV and a
133 current of 300 mA. The monochromator used was Si(311) crystals operating in Quick EXAFS
134 (QEXAFS) mode. The measurements were carried out in fluorescence mode at the Mo K (19999 eV)
135 absorption edge at 298 K using a 9-element Ge detector. Calibration of the monochromator was
136 carried out using a Mo foil previously to the measurements. The acquired data were processed and
137 analyzed using the programs Athena and Artemis [16], respectively, which implement the FEFF6
138 and IFEFFIT codes [17]. Fits were carried out using a *k* range of 3 – 16 Å^{-1} for the MoS$_2$- and 3 – 12 Å^{-1}
139 for the MoS$_3$-based materials and a *R* range of 1.4 – 3.2 Å with multiple *k* weightings of 1, 2 and 3.
140 Different FEFF inputs were used in these fits depending on the materials. A MoS$_3$ model was created
141 based on data from refs [18,19].

142 *2.4. In line photoemission and electrochemical measurements*

143   Measurements were performed in an ultrahigh vacuum (UHV) system that consists of two
144 independent UHV chambers: a preparation/analysis chamber and an electrochemical (EC) chamber.
145 In the preparation/analysis chamber, the samples were prepared using the procedure described
146 above and, subsequently, characterized by X-ray photoemission spectroscopy (XPS). The UHV-EC
147 transfer system, which consists of two manipulators (horizontal and vertical), is connected to the
148 main preparation chamber through a gate valve. The horizontal manipulator is used to transfer the
149 sample from the analysis chamber to the EC chamber, whereas the vertical one allows the sample to
150 be raised to couple it to the electrochemical cell, which is connected to the EC chamber from the top.
151 A custom made PEEK (polyether ether ketone) cell was used for the electrochemical measurements
152 (Figure S1b). A Pt wire was used as counter electrode and an Ag/AgCl/Cl$^-$ (3M KCl) electrode placed
153 in a Luggin capillary was used as reference electrode. The cell was controlled by an Autolab
154 potentiostat running with NOVA 1.8 Software. A 0.1 M HClO$_4$ solution, prepared from high purity
155 reagents (Sigma-Aldrich) and purged with argon gas, was used as the electrolyte. The electrolyte
156 was pumped into the EC cell through a tubing system using a syringe pump (N-1010, Pump Systems
157 Inc.), which allows an accurate control of the flow. The electrolyte inlet consists of a capillary tube
158 (diameter ca. 0.35 mm) placed in the center of the cell, whereas the outlet is constituted by eight
159 holes (diameter 0.5 mm) placed around the central capillary. Prior to the EC measurements, the
160 tubing system was purged with Ar to remove the oxygen and then, it was filled with the electrolyte.
161 The samples were polarized at two different potentials: (a) before HER (+0.18 V vs RHE); and (b) at
162 HER conditions (-0.4 V vs RHE). In this case, in order to see more significant changes in the samples,
163 a more negative potential was selected for the measurement at HER conditions than in the XAS
164 measurements, since the XPS data is not acquired simultaneously to the EC measurement. All the
165 electrochemical experiments were carried out at room temperature, in Ar atmosphere in order to
166 avoid contact of the sample with oxygen, and using a flow rate of 1 mL min^{-1}.
167   The chemical changes induced by the electrochemical work were analyzed by XPS after each
168 electrochemical measurement. Photoemission data were obtained in a custom designed UHV system
169 equipped with a EA 125 Omicron electron analyzer with five channeltrons, working at a base
170 pressure of 10^{-9} mbar. Core level photoemission spectra (S 2p, Mo 3d, C 1s and O 1s regions) were
171 collected at room temperature with a non-monochromatized Al Kα X-ray source (1486.7 eV) and
172 using 0.1 eV steps, 0.5 s collection time and 20 eV pass energy.
173

174 **3. Results and discussion**

175   The MoS$_x$ phase was determined by Raman spectroscopy and the stoichiometry by XPS
176 (Figures 1a and 1b). Raman spectra of both GOQD-MoS$_x$ samples show the characteristic D (1350
177 cm^{-1}), G (1590 cm^{-1}), 2D (2700 cm^{-1}) and D+D'(2900 cm^{-1}) bands of graphene, confirming the presence
178 of GOQDs [20]. Both commercial MoS$_2$ (Aldrich) and GOQD-MoS$_2$ show two bands at 380 cm^{-1} and
179 405 cm^{-1} that correspond to the in-plane E$^1_{2g}$ and out-of-plane A$_{1g}$ vibrational modes (Figure S2),
180 respectively, which are characteristic of 2H-MoS$_2$ [21].In the case of GOQD-MoS$_2$, the broadening
181 and the intensity decrease of the A$_{1g}$ band can be associated with a small number of stacked layers
182 along the *c* axis [22], confirming the limited growth of the MoS$_2$ NPs in presence of GOQDs. The
183 broadening of the E$^1_{2g}$ band is related to the presence of in-plane defects sites, which contributes to
184 the increase of active sites [23,24].The Raman spectrum of GOQD-MoS$_3$, however, shows broad and
185 weak bands due to the amorphous nature of the MoS$_3$ nanoparticles [25,26].The broad bands at
186 282-382 cm^{-1} correspond to the v(Mo-S) stretching and the band at 450 cm^{-1} to the v(Mo$_3$-μ_3S)
187 vibration. The bands at 525 cm^{-1} and 555 cm^{-1} are attributed to S-S stretching from terminal and
188 bridging disulfide bonds (S$_2$)$^{2-}$, respectively, supporting the chain-like structure proposed for
189 amorphous MoS$_3$ [9,25,26].
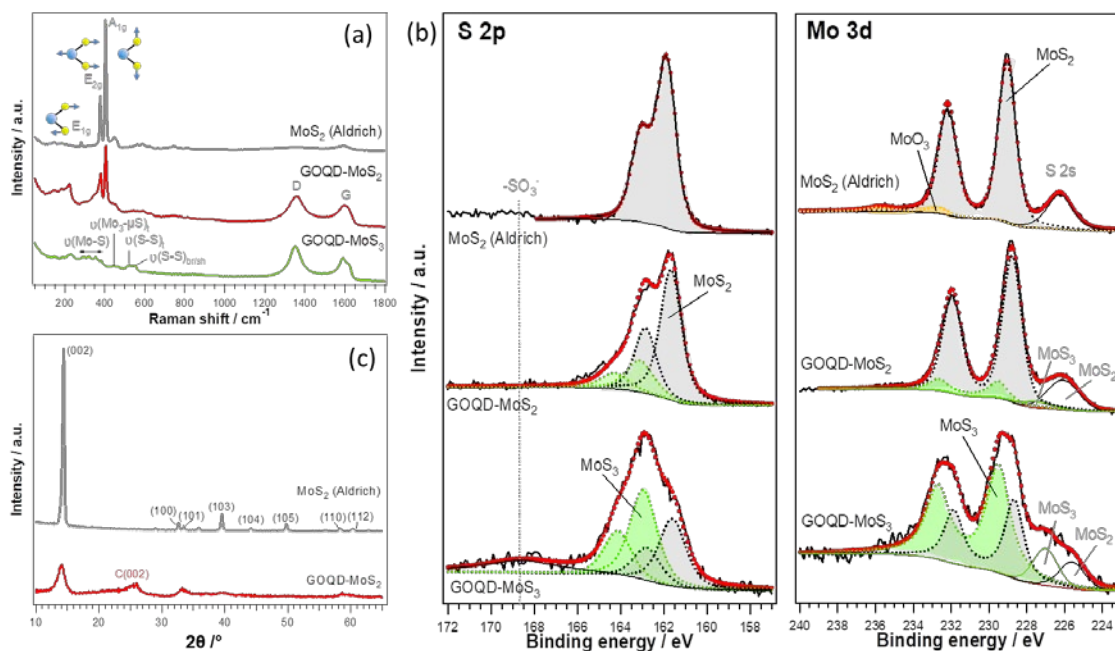
Figure 1. (a) Raman spectra; (b) S 2*p* and Mo 3*d* / S 2*s* photoemission spectra; and (c) XRD patterns for the GOQD-MoS$_x$ (x = 2 and 3) nanohybrids and the commercial MoS$_2$ (Aldrich). GOQD.

In the commercial MoS$_2$, the Mo 3$d_{5/2}$ peak is located at 229.0 eV and the corresponding S 2$p_{3/2}$ at 161.8 eV, which are characteristic of stoichiometric and crystalline MoS$_2$ [27,28]. The Mo 3$d_{5/2}$ photoemission (PE) line also shows a small component at a binding energy (BE) of 232.6 eV, attributed to the presence of MoO$_3$ on the edges due to oxidation by air exposure. GOQD-MoS$_2$ displays the characteristic features of MoS$_2$, confirming the success of the synthesis method; however, in this case, the peaks are slightly wider than in the case of the commercial MoS$_2$, suggesting the residual presence of a small amount of MoS$_3$ (components at 229.5 eV and 163.1 eV in the Mo 3d and S 2p PE, respectively). On the other hand, the Mo 3$d_{5/2}$ PE line of GOQD-MoS$_3$ presents two components at 228.8 and 229.5 eV related to Mo(IV) and Mo(V), respectively. The S 2$p_{3/2}$ PE line also shows two components at 161.8 eV, attributed to divalent sulfide ions (S^{2-}), and 163.0 eV, associated with μ-S$_2^{2-}$ and/or apical S^{2-} [7,9]. The atomic Mo:S ratio calculated from the Mo 3d and S 2p, taking into account the corresponding sensitivity factors, is 1:2.1 for GOQD-MoS$_2$ and 1:2.7 for GOQDs-MoS$_3$. It should be noticed that the BEs for the MoS$_2$ component in the commercial MoS$_2$, both in the Mo 3d and S 2p PE lines, are shifted 0.2 eV towards higher values respect to those for the GOQD-MoS$_x$ samples. This shift is attributed to the higher size of the commercial MoS$_2$ nanoparticles.

Figure 1c compares the X-ray diffraction (XRD) patterns of GOQD-MoS$_2$ and the commercial MoS$_2$. GOQD-MoS$_2$ shows six peaks at 2θ values of 14.1°, 32.9°, 39.5°, 49.7°, 58.4° and 60.3° which are attributed to the (002), (100), (103), (105), (110) and (112) reflections of the hexagonal structure of MoS$_2$ (seen in the XRD pattern of the commercial MoS$_2$) [29].In addition, it shows a broad peak at 2θ = 25° associated with the presence of GOQDs [30,31]. The crystallite size of the MoS$_2$ NPs was determined from the XRD patterns by applying the Scherrer equation to the MoS$_2$(002) peak (Figure S2). The crystallite size calculated for MoS$_2$ and GOQD-MoS$_2$ was 26.5 nm (702 nm^2) and 7.4 nm (43 nm^2), respectively. This confirms once more that, in presence of GOQDs, the growth of MoS$_2$ NPs is inhibited, leading to abundance of exposed edge sites dispersed in the GOQDs matrix. GOQD-MoS$_3$ (not shown), however, did not show reflections, confirming its amorphous nature as seen by Raman spectroscopy. For this reason, it was not possible to determine the actual MoS$_3$ disordered NPs size; however, we expect that it is similar to that of the MoS$_2$ NPs or even smaller (see EXAFS section) due to the lower temperature used in the synthesis.

222   The HER activity of the GOQD-MoS$_x$ nanohybrids was investigated in a standard
223 three-electrode half-cell, using an Ar-saturated 0.5 M H$_2$SO$_4$ solution as electrolyte   Figure 2 shows
224 the polarization curves obtained for GOQD-MoS$_x$, as well as the corresponding Tafel plots. The
225 results for the commercial MoS$_2$ and the carbon paper have also been included for comparison. Two
226 different regions in the polarization curves are observed for all MoS$_x$-based materials. This effect has
227 already been observed in the literature for MoS$_3$ [32]. In that case, the first region was attributed to
228 the formation of reduced molybdenum sulfides, mainly MoS$_2$, whereas the second one was
229 associated with hydrogen evolution. Considering the second process in order to compare the activity
230 of the different materials toward HER, it can be observed that both GOQDs-MoS$_x$ exhibit a very
231 similar activity, which is higher than that showed by the commercial MoS$_2$ in terms of overpotential.
232 However, the three MoS$_x$-based materials show a very similar Tafel slope, indicating that the
233 presence of GOQDs do not modify the kinetics of the process. The enhancement of the activity can
234 be explained by the increase of exposed edge sites due to the coupling with GOQDs that limit the
235 growth of the MoS$_x$ NPs, as confirmed by XRD.
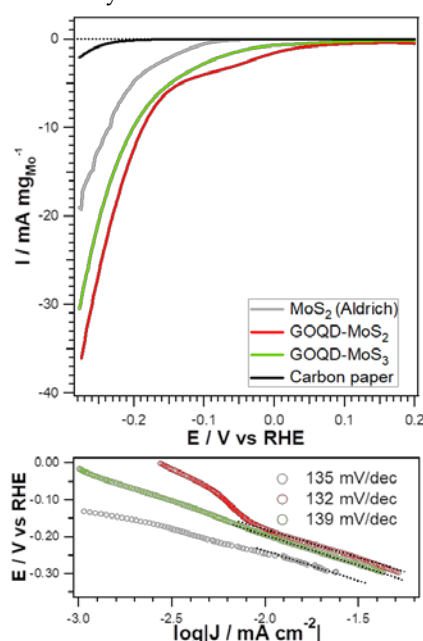
236
237   **Figure 2.** Polarization curves (not IR corrected, upper panel) and corresponding Tafel plots
238 (bottom panel) in deaerated 0.5 M H$_2$SO$_4$ for the GOQD-MoS$_x$ (x = 2 and 3) and commercial MoS$_2$
239 modified electrodes acquired at room temperature and at a scan rate of 5 mV s^{-1}.It is interesting to
240 highlight the similar behavior of the GOQD-MoS$_x$ materials with different composition. To further
241 investigate the origin of the activity of these materials, *operando* XAS characterization was performed
242 under HER conditions. The measurements were carried out at the Mo K edge to establish possible
243 chemical changes as a function of the applied potential. For each material, four different potentials
244 were studied: (i) before HER at +0.18 V$_{RHE}$; (ii) onset of the first slope in the polarization curve (+0.04
245 and -0.07 V$_{RHE}$ for GOQDs-MoS$_x$ and MoS$_2$, respectively); (iii) onset of the second slope in the
246 polarization curve (-0.12 and -0.18 V$_{RHE}$ for GOQDs-MoS$_x$ and MoS$_2$, respectively); and (iv) under
247 HER conditions at -0.23 V$_{RHE}$. The measurements were performed on fresh and aged electrodes.
248 Figures 3a-c show the Fourier transformed extended X-ray absorption fine structure (FT EXAFS)
249 spectra of GOQD-MoS$_x$ and commercial MoS$_2$, whilst the corresponding *k*-space spectra are reported
250 in Figure S3. The MoS$_2$-based materials show two peaks at 2.0 and 2.8 Å (apparent distance), fitted to
251 Mo-S and Mo-Mo interactions, respectively; whereas the MoS$_3$-based sample exhibits the Mo-Mo
252 interaction peak at 2.5 Å. No Mo-O contributions could be fitted for any of the samples, not even in
253 the *ex situ* measured spectra (not shown). This does not exclude the presence of oxide on the edges; if
254 present, as the fraction of Mo atoms that have O neighbors in the first coordination shell is too small
255 to be reliably fitted.
256   The EXAFS data were fitted by using the corresponding MoS$_2$ and MoS$_3$ crystal structures. The
257 MoS$_2$ model consists of a first Mo-S shell with six sulfur atoms at 2.41 Å and a second Mo-Mo shell

258 with six molybdenum atoms at 3.17 Å. For the MoS_3 fitting, the Hibble structure [18] was used,
259 although the Weber structure [33] cannot be excluded. In the Hibble model, Mo atoms interact with
260 only one neighboring Mo atom at 2.77 Å and six S atoms at 2.42 Å [8,34]. The fitting results are
261 summarized in Tables S1-S3. The commercial MoS_2 was fitted with a Mo-S shell with 5.8 sulfur
262 atoms at 2.41 Å and a Mo-Mo shell with 5.7 atoms at 3.17 Å. These values are very close to those of
263 the bulk (6.0 for Mo-S and 6.0 for Mo-Mo), confirming the large size of the MoS_2 particles. Due to the
264 large size, the Mo-O interactions would be negligible. For GOQD-MoS_2, MoS_2 was fitted with a Mo-S
265 shell with 4.1 sulfur atoms at 2.41 Å and a Mo-Mo shell with 2.5 atoms at 3.17 Å. The small
266 coordination number for the Mo-Mo interaction in this sample is due to the smaller NP size
267 compared with that of the commercial MoS_2.
268   Under electrochemical conditions, MoS_2 at +0.18 V (before HER) was fitted with a Mo-S shell
269 with 5.3 sulfur atoms at 2.41 Å and a Mo-Mo shell with 5.1 atoms at 3.17 Å. At more negative
270 potentials (from -0.07 V to -0.23 V vs RHE), no significant changes were observed in the coordination
271 numbers (N) and bond distances (R), and either in the disorder parameter (σ^2), indicating that this
272 material is very stable in this potential range. The fact that no significant changes were observed for
273 this material is also attributed to the large dimension of the NPs and resultant small fraction of
274 atoms on the surface in contact with the electrolyte.
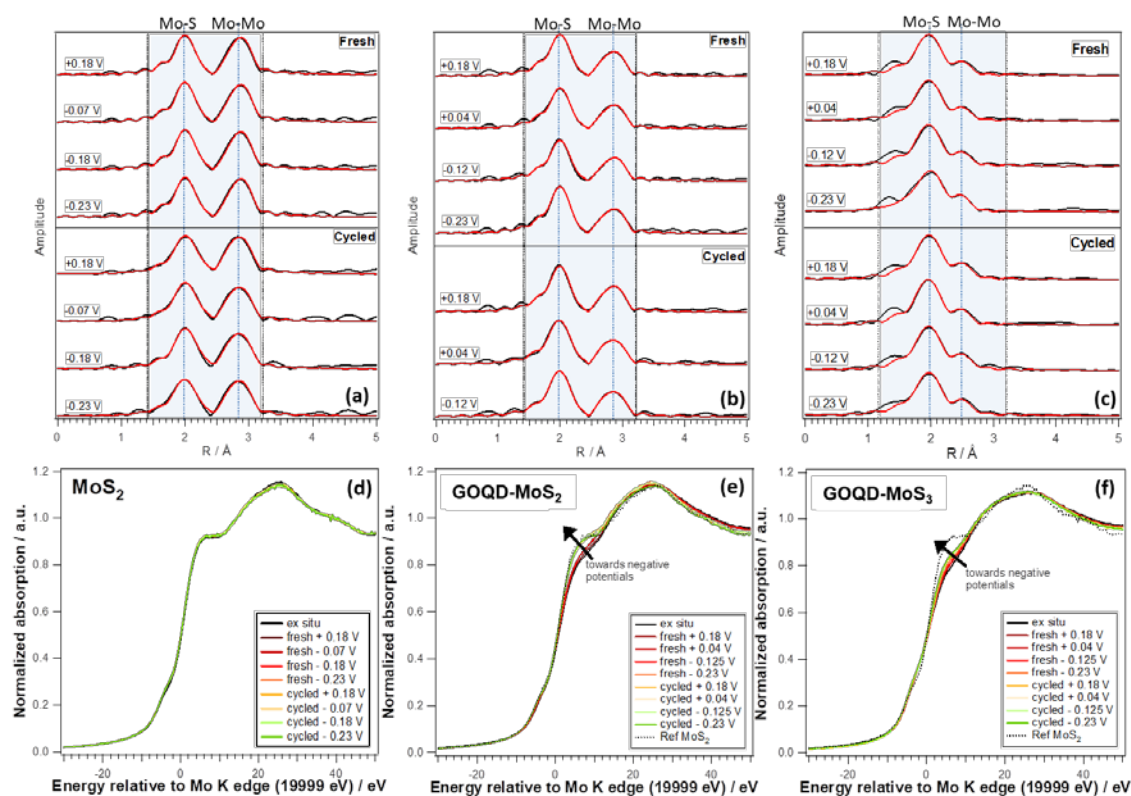
276 **Figure 3.** Fourier transformed EXAFS (a,b,c) and XANES spectra (d,e,f) at Mo K edge for the fresh
277   and aged MoS_2 (Aldrich) (a,d), GOQD-MoS_2 (b,e) and GOQD-MoS_3 (c,f) nanohybrids recorded at
278   different applied potentials. The black and red curves represent the experimental data and the
279   corresponding fit, respectively.

280   The best fit for GOQD-MoS_2 at +0.18 V was obtained with a Mo-S shell with 4.3 sulfur atoms at
281 2.41 Å and a Mo-Mo shell with 2.7 atoms at 3.17 Å. In this case, an increase of the coordination
282 numbers (N_S = 5.0 and N_{Mo} = 3.4) was observed when the HER conditions were reached (E = -0.23 V
283 vs RHE), as well as of the disorder for the Mo-Mo interaction. Taking also into account the X-ray
284 absorption near edge structure (XANES) data reported in Figure 3e, a significant change of the white
285 line at -0.23 V is noted, which shows that the spectral fingerprint matches exactly with that of the
286 MoS_2 reference. This effect could be associated with the reduction under HER conditions of the small

287 fraction of MoS$_3$ (seen by XPS in the as prepared sample) to MoS$_2$ and/or the small amount of oxides
288 present at the edges. The ageing treatment did not caused significant changes in N, R or σ^2 for the
289 MoS$_2$-based materials, indicating that no major restructuring occurred and, therefore, MoS$_2$ was
290 found to be very stable under HER conditions. This stability is attributed to the high crystallinity of
291 the MoS$_2$ NPs obtained.
292   For GOQD-MoS$_3$, the best fit at +0.18 V was obtained by a Mo-S shell with 3.8 sulfur atoms at
293 2.44 Å and a Mo-Mo shell with 1.3 atoms at 2.75 Å, which are in good agreement with those found in
294 the literature for MoS$_3$ [8]. As the potential became more negative, N_S increased while N_{Mo} decreased
295 slightly. In addition, a slight increase in the Mo-Mo bond distance was observed, which could
296 suggest the reduction of the MoS$_3$ NP surface to MoS$_2$. However, the fraction of Mo atoms that
297 change the coordination environment under the HER conditions is too small to observe significant
298 changes in the EXAFS analysis. After the ageing treatment, the same trend in the N_S, N_{Mo} and R_{Mo}
299 was observed. These results suggest that the stoichiometry of MoS$_3$ at the edges could change
300 gradually under HER conditions, whereas the bulk material remains stable, for this reason the
301 changes observed are not very significant. This fact is also supported by the variation of the XANES
302 spectra with the applied potential and the ageing treatment (Figure 3f). Although in the literature it
303 has been stated that MoS$_3$ is not stable under catalytic conditions, being reduced to MoS$_2$ [7,8], our
304 results suggest that only the edges evolve to an structure similar to that of MoS$_2$ while the bulk
305 remains stable as MoS$_3$.
306   In order to further investigate the chemical changes experienced by the MoS$_x$ materials during
307 HER, *in line* XPS/ECl measurements were also performed at two different potentials: (i) before HER
308 (+0.18 V); and under HER conditions (-0.4 V). XPS allows us to track the changes produced only on
309 the surface of the MoS$_x$ NPs, where the electrocatalytic reaction takes place, and to correlate them
310 with the results obtained by XAS.
311   The S 2p and Mo 3d PE spectra for the GOQD-MoS$_x$ samples before and after the
312 electrochemical measurements are displayed in Figure 4, whereas those for the commercial MoS$_2$ can
313 be found in Figure S4. The analysis of the PE lines is summarized in Table S4. As already described
314 above, the components associated with Mo(IV) and Mo(V) were included in the fit of the Mo 3d PE
315 lines, whereas the components related to S^{2-} and bridging S$_2^{2-}$/apical S^{2-} were included in the fit of the
316 S 2p PE lines. After the electrochemical treatments, a new component related to the formation of
317 hydroxides on the surface due to the contact with the electrolyte was included in the fit. It should be
318 noticed that the component associated with the formation of hydroxides was not included in the
319 EXAFS fits since its contribution to the overall signal is negligible.
320   For GOQD-MoS$_2$, no significant changes are observed at +0.18 V, as already seen by XAS. At
321 -0.40 V, the sample is very stable under the catalytic conditions without noticeable changes at this
322 potential. The small discrepancy between the XAS data, which showed a slight reduction of the
323 sample under HER conditions, and the XPS data can be attributed to the fact that in the XPS/EC
324 experiment the sample was prepared *in situ* and not exposed to air before the electrochemical
325 measurements, therefore, no oxidation of the edges occurred. In the case of GOQDs-MoS$_3$, no
326 significant changes occur at +0.18 V, which can also be attributed to the absence of oxidized edges, as
327 explained for the GOQDs-MoS$_2$ sample. However, at HER conditions (E = -0.4 V), an increase of the
328 component associated with S^{2-} in the S 2p line, i.e. the component associated with edges terminated
329 with S-monomers, is observed to the detriment of the component related to the edges terminating
330 with the S-dimer (S$_2^{2-}$). The corresponding increase of Mo(IV) and decrease of Mo(VI) is observed in
331 the Mo 3d line. The atomic Mo:S ratio calculated from XPS at this potential is 1:2.2. It has to be
332 highlighted that if the edges terminate with S-monomers, the local stoichiometry is close to MoS$_2$.
333 Therefore, this result is interpreted as a change of the sulfur terminal sites, from S-dimer (S$_2^{2-}$) to
334 S-monomer (S^{2-}). This change is only produced at the edges of the nanoparticles, since XAS results
335 indicated that the bulk MoS$_3$ NPs are stable under operating conditions, even after the ageing
336 treatment.
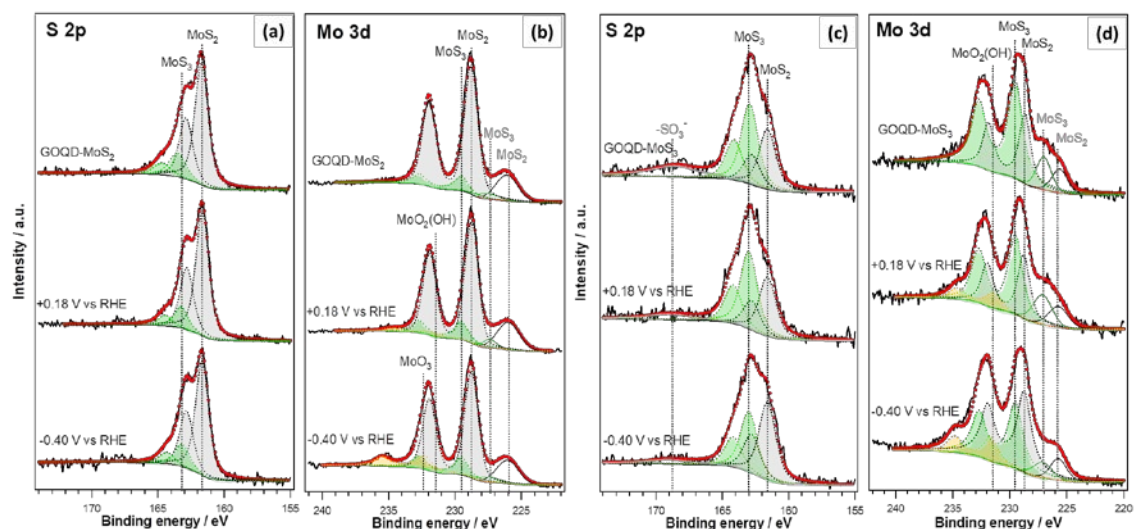
Figure 4. S 2*p* (a,c) and Mo 3*d* (b,d) photoemission lines and their separation into chemically shifted components for GOQD-MoS₂ (a,b) and GOQD-MoS₃ (c,d) before and after the electrochemical measurements in 0.1 M HClO₄ at different potentials. The black and red curves represent the experimental data and the corresponding fit, respectively.

In the literature, different active sites have been proposed; however, our data support the DFT calculations evidencing that the active sites of MoS$_x$ under HER conditions are terminated by S-monomers, confirming the crucial role of S coordination in determining the catalytic activity [7]. Theoretical calculations have also demonstrated that the most favorable mechanism for the hydrogen evolution on MoS₂ involves the first proton adsorption at the S-edge, suggesting that this edge is chemically more active than the Mo-edge [35,36,37]. Therefore, this study confirms that the stable phase of MoS$_x$ in HER conditions entails edges terminated with S-monomers, whose stoichiometry is close to MoS₂. This could explain why, even though both GOQD-MoS$_x$ nanohybrids are active toward the HER, GOQD-MoS₂ exhibit a slightly higher activity in terms of overpotential than GOQD-MoS₃, due to the S-monomer surface termination.

4. Conclusions

We have investigated the chemical stability of GOQD-MoS$_{x, x=2,3}$ nanohybrids by using *operando* X-ray absorption spectroscopy and combined photoemission/electrochemical in line measurements. Our study shows that the GOQD-MoS₂ and GOQD-MoS₃ nanohybrids are both active towards the HER and exhibit a remarkable chemical stability under working conditions, most likely due to the stabilization provided by the GOQD. In addition, our findings show that the edges in the GOQD-MoS₃ nanohybrids (differently than the GOQD-MoS₂) undergo a sulfur coordination change under HER conditions, from S-dimer (S₂²⁻) to S-monomer (S²⁻). This transition has a significant role on the activity of these materials and is probably the reason of the similar activity of both MoS$_x$ phases.

In conclusion, our work provides general information about the experimental tools that allow for an optimal characterization of electrocatalytic materials, showing that the knowledge gained from the synergistic application of different investigation techniques allows to address fundamental questions in energy materials and conversion research.

377 **Conflicts of Interest:** "The authors declare no conflict of interest."

378 **References**

1. Helm M.L.; Stewart M.P.; Bullock R.M.; DuBois M.R.; DuBois D.L. A Synthetic Nickel Electrocatalyst with a Turnover Frequency Above 100,000 s^{-1} for H$_2$ Production. *Science* **2011**, *333*, 863-866.

2. Walter M.G.; Warren E.L.; McKone J.R.; Boettcher S.W.; Mi Q.X.; Santori E.A.; Lewis N.S. Solar Water Splitting Cells. *Chem. Rev.* **2010**, *110*, 6446-6473.

3. Tran P.D.; Le Goff A.; Jousselme H.J.B.; Guillet N.; Palacin S.; Dau H.; Fontecave M.; Artero V.. Noncovalent Modification of Carbon Nanotubes with Pyrene-Functionalized Nickel Complexes: Carbon Monoxide Tolerant Catalysts for Hydrogen Evolution and Uptake. *Angew. Chem., Int. Ed.* **2011**, *50*, 1371-1374.

4. Jaramillo T.F.; Jorgensen K.P.; Bonde J.; Nielsen J.H.; Horch S.; Chorkendorff I. Identification of Active Edge Sites for Electrochemical H$_2$ Evolution from MoS$_2$ Nanocatalysts. *Science* **2007**, *317*, 100-102.

5. Merki D.; Hu X.L. Recent developments of molybdenum and tungsten sulfides as hydrogen evolution catalysts. *Energy Environ. Sci.* **2011**, *4*, 3878-3888.

6. Wu L.; Longo A.; Dzade N.Y.; Sharma A.; Hendrix M.M.R.M.; Bol A.A.; de Leeuw N.H.; Hensen E.J.M.; Hofmann J.P. The Origin of High Activity of Amorphous MoS$_2$ in the Hydrogen Evolution Reaction. *ChemSusChem* **2019**, *12*, 4383-4389.

7. Sanchez Casalongue H.G., Benck J.D., Tsai C., Karlsson R.K.B., Kaya S., Ng M.L., Pettersson L.G.M., Abild-Pedersen F., Nørskov J.K., Ogasawara H., Jaramillo T.F., Nilsson A. Operando characterization of an amorphous molybdenum sulphide nanoparticle catalyst during hydrogen evolution reaction, *J Phys. Chem. C* **2014**, 118, 29252-29259.

8. Lassalle-Kaiser B.; Merki D.; Vrubel H.; Gul S.; Yachandra V.K.; Hu X.; Yano J. Evidence from in situ X-ray absorption spectroscopy for the involvement of terminal disulfide in the reduction of protons by an amorphous molybdenum sulfide electrocatalyt, *J. Am. Chem. Soc.* **2015**, *137*, 314-321.

9. Tran P.D.; Tran P.; Orio T.; Torelli M.S.; Truong Q.D.; Nayuki K.; Sasaki Y.; Chiam S.Y.; Yi R.; Honma I.; Barber J.; Artero V. Coordination polymer structure and revisited hydrogen evolution catalytic mechanism for amorphous molybdenum sulphide. *Natur. Mater.* **2016**, *15*, 640–646.

10. Huang Y.; Nielsen R.J.; Goddard W.A.; Soria M.P. The Reaction Mechanism with Free Energy Barriers for Electrochemical Dihydrogen Evolution on MoS$_2$. *J. Am. Chem. Soc.* **2015**, *137*, 20, 6692-6698.

11. Ting L.R.L., Deng Y., Ma L., Zhang Y.-J., Peterson A.A., Yeo B.S. Catalytic Activities of Sulfur Atoms in Amorphous Molybdenum Sulfide for the Electrochemical Hydrogen Evolution Reaction. *ACS Catal.* **2016**, *6*, 2, 861-867.

12. Xie J.; Xie J.; Zhan J. g; Li S.; Grote F.; Zhang X.; Zhang H.; Wang R.; Lei Y.; Pan B.; Xie Y. Controllable Disorder Engineering in Oxygen-Incorporated MoS$_2$ Ultrathin Nanosheets for Efficient Hydrogen Evolution. *J. Am. Chem. Soc.* **2013**, *135*, 47, 17881-17888.

13. Seo B.; Jung G.Y.; Lee S.J.; Baek D.S.; Sa Y.J.; Ban H.W.; Son J.S.; Park K.; Kwak S.K.; Joo S.H. Monomeric MoS$_4^{2-}$-Derived Polymeric Chains with Active Molecular Units for Efficient Hydrogen Evolution Reaction. *ACS Catal.* **2020**, *10*, 1, 652-662.

14. Geim A.K.; Novoselov K.S. The rise of graphene. *Nat. Mater.* **2007**, *6*, 183-191.

15. Wise A.M.; Richardson P.W.; Price S.W.T.; Chouchelamane G.; Cavillo L.; Hendra P.J.; Toney M.F.; Russell A.E. Inhibitive effect of Pt on Pd-hydride formation of Pd@Pt core-shell electrocatalysts: An in situ EXAFS and XRD study, *Electrochim. Acta*, **2018**, *262*, 27-38

16. Ravel B.; Newville M.J. ATHENA, ARTEMIS, HEPHAESTUS: data analysis for X-ray absorption spectroscopy using IFEFFIT. *Synchrotron Rad*. **2005**, *12*, 537-541.

17. Newville, M. EXAFS analysis using FEFF and FEFFIT. *J. Synchrotron Rad*. **2001**, *8*, 96-100.

18. Hibble S.J.; Rice D.A.; Pickup D.M.; Beer M.P. Mo K-edge EXAFS and S K-edge absorption studies of the amorphous molybdenum sulphides $MoS_{4.7}$, MoS_3, and $MoS_3 \cdot nH_2O$ (n ~ 2), *Inorg. Chem.* **1995**, 34, 5109-5113.

19. Walton R.I.; Dent A.J.; Hibble S.J. In situ investigation of the thermal decomposition of ammonium tetrathiomolybdate using combined time-resolved X-ray absorption spectroscopy and X-ray diffraction, *Chem. Mater.* **1998**, *10*, 3737-3745.

20. Dikin D.A.; Stankovich S.; Zimney E.J.; Piner R.D.; Dommett G.H.B.; Evmenenko G.; Nguyen S.T.; Ruoff R.S. Preparation and characterization of graphene oxide paper. *Nature* 448, **2007**, 457-460.

21. Li H.; Zhang Q.; Yap C.C.R.; Tay B.K.; Edwin T.H.T.; Olivier A.; Baillargeat D. From Bulk to Monolayer MoS_2: Evolution of Raman Scattering. *Adv. Funct. Mater.* **2012**, *22*, 1385-1390.

22. Lee C.; Yan H.; Brus L.E.; Heinz T.F.; Hone J.; Ryu S. Anomalous Lattice Vibrations of Singleand Few-Layer MoS_2. *ACS Nano* **2010**, *4*, 2695-2700.

23. Miao J.; Xiao F.-X.; Yang H.B.; Khoo S.Y.; Chen J.; Fan Z.; Hsu Y.-Y.; Chen H.M.; Zhang H.; Liu B. Hierarchical Ni-Mo-S nanosheets on carbon fiber cloth: A flexible electrode for efficient hydrogen generation in neutral electrolyte. *Sci. Adv.* **2015**, 1:e1500259.

24. Zhang X.; Qiao X.-F.; Shi W.; Wu J.-B.; Jiang D.-S.; Tan P.-H. Phonon and Raman scattering of two-dimensional transition metal dichalcogenides from monolayer, multilayer to bulk material. *Chem. Soc. Rev.,* **2015**, *44*, 2757-2785.

25. Chang C.H.; Chan S.S. Infrared and Raman studies of amorphous MoS_3, and poorly crystalline MoS_2, *J. Catal.* 72, **1981**, 139-148.

26. Sourisseau C.; Gorochov O.; Schleich D.M. Comparative IR and Raman studies of various amorphous MoS_3 and Li_xMoS_3 phases, *Mater. Sci. Eng.* **1989**, *B3,* 113-117.

27. Yan Y.; Xia B.; Ge X.; Liu Z.; Wang J.-Y.; Wang X. Ultrathin MoS_2 nanoplates with rich active sites as highly efficient catalyst for hydrogen evolution, *Appl. Mater. Interfaces* **2013**, *5*, 12794-12798.

28. Chang Y.-H.; Lin Ch.-T.; Chen T.-Y.; Hsu Ch.-L.; Lee Y.-H., Zhang W., Wei K.-H., Li L.-J. Highly efficient electrocatalytic hydrogen production by MoS_x grown on graphene-protected 3D Ni foams, *Adv. Mater.* **2013**, *25*, 756-760.

29. Chung D.Y.; Park S.-K.; Chung Y.-H.; Yu S.-H.; Lim D.-H.; Jung N.; Ham H.C.; Park H.-Y.; Piao Y.; Yoo S.J.; Sung Y.-E. Edge-exposed MoS_2 nano-assembled structures as efficient electrocatalysts for hydrogen evolution reaction. *Nanoscale* 6, **2014**, 2131-2136.

30. Li L.; Wu G.; Yang G.; Peng J.; Zhao J.; Zhu J.-J. Focusing on luminescent graphene quantum dots: current status and future perspectives. *Nanoscale* **2013**, *5*, 4015-4039.

31. Wang L.; Wang Y.; Xu T.; Liao H.; Yao Ch.; Liu Y.; Li Z.; Chen Z.; Pan D.; Sun L.; Wu M. Gram-scale synthesis of single-crystalline graphene quantum dots with superior optical properties. *Natur. Commun.* **2014**, *5*, 5357.

32. Vrubel H.; Merki D.; Hu X. Hydrogen evolution catalysed by MoS_3 and MoS_2 particles, *Energy Environ. Sci.* **2012**, *5*, 6136-6144.

33. Weber Th.; Muijsers J.C.; Niemantsverdriet J.W. Structure of Amorphous MoS_3. *J. Phys. Chem.* **1995**, 99, 9194-9200.

34. Cramer S.P.; Liang K.S.; Jacobson A.J.; Chang C.H.; Chianelli R.R. EXAFS studies of amorphous molybdenum and tungsten trisulfides and triselenides, *Inorg. Chem.* **1984**, *23*, 1215-1221.

35. Huang Y.; Nielsen R.J.; Goddard W.A.; Soriaga M.P. The reaction mechanism with free energy barriers for electrochemical dihydrogen evolution on MoS_2, *J. Am. Chem. Soc.* **2015**, *137*, 6692-6698.

36. Bollinger M.V.; Jacobsen K.W.; Norskov J.K. Atomic and electronic structure of MoS_2 nanoparticles. *Phys.Rev.* **2003**, *B 67*, 085410.

37. Raybaud P.; Hafner J.; Kresse G.; Kasztelan S.; Toulhoat H. Structure, energetics, and electronic properties of the surface of a promoted MoS_2 catalyst: An ab initio local density functional study. *J. Catal*. **2000,** *190*, 128-143.